

Dilute lattice doping of Cu-64 into 2D-nanoplate; its impact on radio-labeling efficiency and stability for target selective PET imaging

Sairan Eom

Ewha Womans University

Min Hwan Kim

Korea Institute of Radiological and Medical Sciences

Ranji Yoo

Korea Institute of Radiological and Medical Sciences

Goeun Choi

Dankook University

Joo Hyun Kang

Korea Institute of Radiological and Medical Sciences

Yong Jin Lee

Korea Institute of Radiological and Medical Sciences

Jin-Ho Choy (✉ jhchoy@dankook.ac.kr)

Dankook University

Research Article

Keywords: Quintinite, Radio-labeled nanoplates, Radio-labeling efficiency and stability, Radio-imaging and diagnostic nano-device, Positron emission tomography

Posted Date: April 20th, 2022

DOI: <https://doi.org/10.21203/rs.3.rs-1542004/v1>

License: © ⓘ This work is licensed under a Creative Commons Attribution 4.0 International License.

[Read Full License](#)

Abstract

Background:

Positron emission tomography (PET) in nuclear medicine provides useful information for tumor diagnosis due to its high sensitivity and quantitiveness on biochemical and physiological changes in *in-vivo* system. Radioisotope-labeled materials developed for PET imaging still have decisive weakness, since they are low in labeling efficiency and labeling stability.

Results

Quintinite nanoplate (^{64}Cu -QT-NP) isomorphically substituted with ^{64}Cu , as the positron emission tomography (PET) imaging material, was prepared *via* two-step processes. The ^{64}Cu labeling efficiency of 99% was realized, for the first time, by immobilizing the ^{64}Cu radioisotope directly in the octahedral site of 2 dimensional (2D) quintinite lattice. Furthermore, the ^{64}Cu labeling stability of ^{64}Cu -QT-NPs was also achieved more than $\sim 99\%$ in various solutions such as saline, phosphate-buffered saline (PBS), and other biological media (mouse and human serums). In *in-vivo* xenograft mice model, the passive targeting behavior of ^{64}Cu -QT-NPs into tumor tissue based on enhanced permeability and retention (EPR) effect was also demonstrated by parenteral administration, and successfully visualized using positron emission tomography (PET) scanner. For enhancing the tumor tissue selectivity, the bovine serum albumin (BSA) was coated on ^{64}Cu -QT-NPs to form ^{64}Cu -QT-NPs/BSA, resulting in better colloidal stability and longer blood circulation time, which was eventually evidenced by the 2-fold higher tumor uptake rate when intravenously injected in an animal model.

Conclusions

The present ^{64}Cu -QT-NPs/BSA with tumor tissue selectivity could be an advanced nano-device for radio-imaging and diagnosis as well.

Background

In the last decades, precise diagnosis of disease has been an important issue in medicine. In particular, researches on various imaging materials for early detection of cancer have been carried out to enhance their sensitivity, bioaffinity, and stability in the human body [1–9]. At the same time, molecular imaging techniques have been also constantly advancing, and contributing to the development of life and medical sciences. For example, nuclear imaging techniques, including scintigraphy, positron emission tomography (PET), and single-photon emission computed tomography (SPECT) have been extensively studied, since they can provide useful information for tumor diagnosis by tracing biochemical and

physiological changes in *in-vivo* systems thanks to their high sensitivity and quantitiveness without any tissue penetration limit [10, 11].

To obtain nuclear imaging detection, radioisotopes, such as ^{18}F , ^{64}Cu , ^{68}Ga , and $^{99\text{m}}\text{Tc}$, were used in combination with a variety of materials including chelators, metal oxides, liposomes, dendrimers, and layered compounds [12–22]. Out of various radioisotopes, ^{64}Cu was considered as an useful radioisotope for both PET imaging and targeted radiotherapy due to its long half-life (12.7 h) enough to synthesize a various size of molecular assemblies and nanoparticles for radiopharmaceutical materials, and its decay scheme of β^+ (18%), β^- (38.5%), and electron capture (ϵ , 43.5%) as shown in Fig S1 [23–24]. The ^{64}Cu radionuclide has been commonly produced by proton irradiation in medical cyclotron using $^{64}\text{Ni}(p, n)^{64}\text{Cu}$ nuclear reaction ($_{28}^{64}\text{Ni} + {}_1^1\text{p} \rightarrow {}_{29}^{64}\text{Cu} + {}_0^1\text{n}$), as one of the widely used nuclear reactions due to its high production yield and purity [25–27]. The thus produced ^{64}Cu has been further applied to develop a variety of ^{64}Cu -labeled complexes and/or nanomaterials for PET imaging [14, 23, 28–33]. Typically, various chelating molecules, such as 1,4,7,10-tetraazacyclododecane-1,4,7,10-tetraacetic acid (DOTA), and 1,4,7-triazacyclononane-1,4,7-triacetic acid (NOTA), were used to bind ^{64}Cu radionuclides, and the ^{64}Cu -chelators were further conjugated with nanoparticles, and/or targeting moieties such as antibodies, proteins, peptides, and other biologically relevant small molecules [28, 29]. However, they turned out to be quite low in radiolabeling efficiency (Table S1) and chemically unstable in *in-vitro* and *in-vivo* due to the weak bonding interaction between ^{64}Cu and chelators [30–33]. For example, the radiolabeling efficiency of NOTA, known as a hexadentate N_3O_3 chelator, for ^{64}Cu was obtained with 65 ~ 70 % [30]. A radiolabeling efficiency of 71.9 % was also reported for ^{64}Cu -DOTA conjugated with monoclonal antibody (mAb), where the ^{64}Cu radionuclide was made of cross-bridged bicyclic tetraamine of DOTA [31]. To overcome such a weak interaction, some bifunctional chelators were developed, but a harsh condition was required to prepare ^{64}Cu -chelators. Apart from that, the labeling stability was also still insufficient as well [28]. For PET applications in *in-vivo*, it has long been required to develop chemically stable ^{64}Cu complexes and/or nanomaterials with externally adsorbed ^{64}Cu -derivatives [32, 33].

On the other hand, quintinite ($[\text{Mg}_2\text{Al}(\text{OH})_6]^{1+}[\text{CO}_3^{2-}]_{0.5} \cdot 1.5\text{H}_2\text{O}$, QT), different from hydrotalcite ($[\text{Mg}_3\text{Al}(\text{OH})_8]^{1+}[\text{CO}_3^{2-}]_{0.5} \cdot 2\text{H}_2\text{O}$, HT) known as an anionic clay, has attracted a great attention in nanomedicine due to its excellent biocompatibility, controllable drug-loading capacity, enhanced cellular permeability, and tumor targeting property [34–40]. Its lamellar structure comprises of brucite ($\text{Mg}(\text{OH})_2$) layers, where magnesium cations (Mg^{2+}) are octahedrally coordinated with six OH^- ions. In QT structure, however, positive layer charge can be generated by replacing divalent Mg^{2+} in the brucite lattice with trivalent aluminum cations (Al^{3+}), and thus the chemical composition of QT can be described by the general formula of $[\text{Mg}_2\text{Al}(\text{OH})_6]^{1+}[\text{CO}_3^{2-}]_{0.5} \cdot n\text{H}_2\text{O}$. If the chemical composition of QT was modified, a series of layered double hydroxide (LDH) phases could be formed with a general formula of $[\text{M}^{2+}_{1-x}\text{M}^{3+}_x(\text{OH})_2]^{x+}[\text{A}^{m-}]_{x/m} \cdot n\text{H}_2\text{O}$ [41–43], where M^{2+} and M^{3+} are divalent and trivalent metal cations such as

Mg^{2+} , Ca^{2+} , Zn^{2+} , Co^{2+} , Cu^{2+} , Ni^{2+} , etc., and Al^{3+} , Fe^{3+} , Co^{3+} , Ga^{3+} , etc., and A^{m-} describes the interlayer anions such as $(CO_3)^{2-}$, $(NO_3)^{1-}$, Cl^{1-} , etc., which can be easily changed depending upon synthetic conditions. One thing to underline here is that interlayer anions are exchangeable so that various negatively charged biofunctional molecules such as anticancer drugs, DNAs, and RNAs can be immobilized in the interlayer space by simple ion exchange reaction [44–50].

Radioisotopes, like ^{64}Cu , ^{57}Co , ^{68}Ga , etc. with divalent or trivalent cations in aqueous solution, could be isomorphically substituted into the octahedral sites of QT lattice under controlled synthetic conditions. Recently, several attempts have been made to study that the radioisotopes label with QT-NPs for radio-imaging and diagnosis [51, 52]. For example, chelator-free nanoparticles, in which ^{64}Cu radioisotopes were adsorbed on the external surface of QT-NPs by simple mixing, have been developed for PET imaging [51]. Thus prepared ^{64}Cu adsorbed QT-NPs were, however, determined to be extremely poor in ^{64}Cu labeling efficiency of only 59.0%, which were reduced down 16.6% even after bovine serum albumin (BSA) coating on them. This attempt is, therefore, considered as a failure one, due to the weak chemical bonding interaction between ^{64}Cu radioisotopes and QT-NPs. One more thing to note here is that the physisorbed radioisotope was found to be partly transformed to impurity phase such as $^{64}Cu^{2+}$ -hydroxycloide, which fell off easily from the external surface of QT-NPs. If this was applied to a patient, an additional toxicity could be expected due to the fact that a large amount of QT-NPs and toxic impurity should be simultaneously injected in order to meet the required radiolabeling efficiency. It is, therefore, highly required to improve the radiolabeling efficiency and chemical stability of radioisotopes immobilized on QT-NPs without any impurities.

In the present study, we attempted to develop biocompatible and chemically stable ^{64}Cu -labeled QT-NPs as follows; (1) $^{64}Cu^{2+}$ ion was isomorphically substituted in the octahedral site of QT lattice *via* two-step processes, co-precipitation and subsequent hydrothermal treatment, to form ^{64}Cu -labeled QT-NPs (^{64}Cu -QT-NPs) (Fig. 1a), and then (2) ^{64}Cu -QT-NPs were coated with BSA (^{64}Cu -QT-NPs/BSA) to enhance the circulation time in blood stream when injected (Fig. 1b). And the radiolabeling stability of ^{64}Cu -QT-NPs and ^{64}Cu -QT-NPs/BSA was compared with that of ^{64}Cu -ads-QT-NPs (^{64}Cu radioisotope physisorbed on QT-NPs) and ^{64}Cu -ads-QT-NPs/BSA (the BSA coated one) as the control groups (Fig. S2). Our isomorphically substituted ^{64}Cu samples, ^{64}Cu -QT-NPs and ^{64}Cu -QT-NPs/BSA, were investigated not only for the radiolabeling efficiency and the chemical stability of ^{64}Cu radioisotope, but also for the tumor targeting and imaging efficiency in xenograft mice model.

Methods

Materials

Magnesium nitrate hexahydrate ($Mg(NO_3)_2 \cdot 6H_2O$), aluminum nitrate nonahydrate ($Al(NO_3)_3 \cdot 9H_2O$), sodium carbonate (Na_2CO_3), and sodium hydroxide (NaOH) were purchased from Daejung Chemical and

Metals (Republic of Korea). Copper chloride dihydrate ($\text{CuCl}_2 \cdot 2\text{H}_2\text{O}$) and bovine serum albumin (BSA) were provided by Sigma-Aldrich (USA). All the reagents were used without further purification. The radioactive copper isotope (^{64}Cu) was produced at the Korea Institute of Radiologic and Medical Sciences (KIRAMS) using a 50 MeV cyclotron (Scantronics) and enriched with nickel isotope (^{64}Ni , 99%; Isoflex) as the target material [25] based on the $^{64}\text{Ni}(p, n)^{64}\text{Cu}$ nuclear reaction ($_{28}^{64}\text{Ni} + {}_1^1\text{p} \rightarrow {}_{29}^{64}\text{Cu} + {}_0^1\text{n}$).

Synthesis of the ^{64}Cu radioisotope labeled samples, the isomorphically substituted ^{64}Cu into QT-NPs, ^{64}Cu -QT-NPs and the BSA coated, ^{64}Cu -QT-NPs/BSA

All the experiments with ^{64}Cu radioisotope including its production were carried out at the KIRAMS according to the safety guideline of Nuclear Safety and Security Commission (NSSC) and Korea Institute of Nuclear Safety (KINS). The unit of radioactivity, the number of spontaneous nuclear disintegrations per unit time, was expressed in becquerels (Bq) in accordance with the international normative ISO 19461-1:2018(en). For doping ^{64}Cu radioisotope into QT to form ^{64}Cu -QT-NPs, first of all, ^{64}Cu radioisotope with a special activity of approximately 142.5 MBq/ng (9.03 GBq/nmol) [53] was produced as a form of $^{64}\text{CuCl}_2$ using a 50 MeV cyclotron as follows [25]; (1) 99% of enriched ^{64}Ni (10 mm plating diameter) on gold foil was irradiated by the proton beam in cyclotron with 30–50 μA at 18 MeV for an hour, and then (2) the ^{64}Ni target was hydrothermally dissolved in hydrochloric acid (HCl, 6.0 M, 10mL) at 80°C. (3) Finally, ^{64}Cu radioisotope was separated from thus dissolved solution using purification process with about 740 MBq/h of production yield by ion exchange resin in plastic case (PEEK, dimension as 1 4 cm). And then, the $^{64}\text{CuCl}_2$ solution (2 mL) with 740 MBq (81.94 pmol of ^{64}Cu radioisopes) was evaporated under Ar gas stream and re-dissolved in 200 μL of 0.1M HCl. Thus prepared $^{64}\text{CuCl}_2$ solution (740 MBq) was directly mixed with a solution (1 mL) containing reactant metal salts, Mg^{2+} (1 μmol) and Al^{3+} (0.5 μmol), which was then titrated with an aqueous one of NaOH (50 mM) and Na_2CO_3 (20 mM) under a vigorous stirring condition until pH reached to 10.0, as shown in Fig.1a; the nominal molar ratio for the sample, ^{64}Cu -QT-NPs, was 1.0:0.5:0.000082 (Mg:Al: ^{64}Cu). Thus prepared suspension was aged for 10 min, and then the white precipitate was collected *via* centrifugation, washed with deionized water, re-dispersed, and further hydrothermally treated at 100°C for 3 h to obtain a desired colloidal suspension of ^{64}Cu -QT-NPs. Based on this co-precipitation and subsequent hydrothermal route, the radioisotope ^{64}Cu was successfully stabilized in the octahedral site of QT lattice. To enhance the colloidal stability of thus prepared ^{64}Cu -QT-NPs, BSA was further coated on them to form ^{64}Cu -QT-NPs/BSA simply by mixing a suspension of ^{64}Cu -QT-NPs and a solution of 0.5 mL BSA (50 mg/mL) under a vigorous stirring condition for 2 h at room temperature. Half (~370 MBq) of the total ^{64}Cu -QT-NPs suspension was used to prepare the BSA coated sample, ^{64}Cu -QT-NPs/BSA, due to the limitation of the total amount of ^{64}Cu radioisotope used.

In order to evaluate the radiolabeling efficiency by the amount of ^{64}Cu radioactivity, 0.5 μmol of ^{64}Cu -QT-NPs was used to prepare the samples with different doses of ^{64}Cu radioactivity of 74, 185, 370, and 740

MBq, corresponding to 8.19, 20.49, 40.97, and 81.94 pmol of ^{64}Cu . In addition, considering the detection range of radioactivity measuring equipment at each experimental step, a reasonable amount of radiolabeled samples was used to evaluate in *in-vitro* and *in-vivo* studies as follows; ~ 3.7 MBq (~ 5 nmol of QT, ~ 0.41 pmol of ^{64}Cu) of the prepared samples for the radiolabeling stability, ~ 0.37 MBq (~ 0.5 nmol of QT, ~ 0.041 pmol of ^{64}Cu) for *in-vitro* cell study, and ~ 1.11 MBq (~ 1.5 nmol of QT, ~ 0.25 pmol of ^{64}Cu) for *in-vivo* biodistribution study, and ~ 11.1 MBq (~ 15 nmol of QT, ~ 2.5 pmol of ^{64}Cu) for *in-vivo* PET imaging study.

Synthesis of the non-radioactive Cu doped samples, the isomorphically substituted Cu into QT-NPs, Cu-QT-NP and the BSA coated, Cu-QT-NPs/BSA

Since the radioisotope was limitedly produced less than μmol level, only a small amount of radioisotope labeled phases was available. To secure an enough amount of samples for various experiments, we have also prepared nonradioactive samples, Cu-QT-NPs and Cu-QT-NPs/BSA, along with the radioisotope labeled. Cu-QT-NPs with a molar ratio of 0.999:0.5:0.001 (Mg:Al:Cu, Cu^{2+} was doped in the 0.1% of Mg^{2+} sites) were prepared by co-precipitation at room temperature, and subsequent hydrothermal reaction; a mixed solution (100 mL) of $\text{Mg}(\text{NO}_3)_2 \cdot 6\text{H}_2\text{O}$ (9.99 mmol), $\text{Al}(\text{NO}_3)_3 \cdot 9\text{H}_2\text{O}$ (5 mmol), and $\text{CuCl}_2 \cdot 2\text{H}_2\text{O}$ (0.01 mmol) was titrated with an aqueous solution of NaOH (50 mM) and Na_2CO_3 (20 mM) up to pH = 10.0 under vigorous stirring. The resulting suspension was aged for 10 min and subsequently treated under hydrothermal condition at 100°C for 3 h. And thus prepared Cu-QT-NPs precipitate was mixed with a BSA solution under vigorous stirring for 2 h to form Cu-QT-NPs/BSA.

Characterization

The crystal structure analysis for all the samples was performed by powder X-ray diffractometer (D/Max 2000, Rigaku) with Ni-filtered Cu K α radiation ($\lambda = 1.5418 \text{ \AA}$) from 5° to 70° operating at 40 kV and 30 mA, with a scanning rate of $2^\circ/\text{min}$. In order to obtain XRD patterns from a very small amount (~ nmol level) of ^{64}Cu -QT-NPs and ^{64}Cu -QT-NPs/BSA, each sample was very carefully dropped on the surface of XRD sample holder and slowly dried in a drying oven at 60°C . According to the XRD patterns for those samples, the peak intensity was rather lowered in a higher range of 2 theta angle around $30^\circ \sim 70^\circ$ due to the peak broadening effect, but the peaks seemed to be better resolved in the 2 theta region of $5^\circ \sim 30^\circ$. The morphology and particle size were analyzed with a scanning electron microscope (SEM, JEOL JSM-6700F), and the particle size distribution and zeta potential were also measured on the basis of DLS method with Zetasizer Nano (Malvern); only the nonradioactive samples, Cu-QT-NPs and Cu-QT-NPs/BSA, prepared under the same synthetic condition of ^{64}Cu -QT-NPs and ^{64}Cu -QT-NPs/BSA, were analyzed due to the limited amount of the radioisotope labeled samples.

In-vitro ^{64}Cu labeling efficiency and labeling stability

To determine the labeling efficiency for all the samples, each suspension was centrifuged using a filter tube (MWCO 10k; Millipore) at 13000 rpm for 30 min. The radioactivity of each precipitate and each

supernatant was measured using a radioisotope calibrator (CRC®-55tR, Capintec, Inc., USA). The labeling efficiency (%) was derived from the measured data according to the following Eq. (1);

$$\text{Labeling efficiency} = \frac{\text{Radioactivity of isolated particles}}{\text{Radioactivity of supernatants} + \text{Radioactivity of isolated particles}} \times 100$$

1

This procedure was repeated three times to ensure accurate results.

The labeling efficiency and stability of each precipitate were also determined by radio-thin layer chromatography (radio-TLC) (Bioscan, AR-2000) using a 20 mM sodium citrate/50 mM ethylenediaminetetraacetic acid (EDTA) solution (pH = 5.5) as a mobile phase.

The labeling stability study of ^{64}Cu -QT-NPs and ^{64}Cu -QT-NPs/BSA was carried out in various media including saline, PBS, mouse serum, and human serum. The sample suspension (3.7 MBq/100 μL) was separately mixed with each media (100 μL), respectively. The mixtures of suspension and media were incubated at 37°C for 1, 3, 12, and 36 h, respectively. And then the mixture in each filter tube was separated into precipitates and supernatants by the centrifugation at 13000 rpm for 30 min. Finally the radioactivity of isolated precipitates and supernatants was measured using a radioisotope calibrator, and the procedure was repeated three times to ensure accurate results. The labeling stability (%) was also estimated from the Eq. (1) with respect to time.

In-vitro cytotoxicity and cellular uptake behavior of ^{64}Cu -QT-NPs and ^{64}Cu -QT-NPs/BSA

The human breast cancer cell line (MDA-MB-231) was purchased from the American Type Culture Collection (ATCC) and cultured in the Roswell Park Memorial Institute (RPMI) 1640 medium (WelGENE, Republic of Korea) with 10% fetal bovine serum (FBS) and 1% antibiotics (both by Invitrogen, USA) under an atmosphere of 5% CO_2 and 95% air at 37°C.

The cytotoxicity for ^{64}Cu -QT-NPs and ^{64}Cu -QT-NPs/BSA was measured on the basis of trypan blue exclusion assay; the cells (5×10^5 cells/well) incubated for overnight at 37°C under a 5% CO_2 atmosphere were treated, respectively, by ^{64}Cu -QT-NPs and ^{64}Cu -QT-NPs/BSA with a radioactivity of 0.37 MBq. After incubation for 0.5, 1, 2, 4, 16, and 24 h, the cells were washed twice with ice-cold PBS and detached with 0.1% trypsin. The detached cells were collected in the media, and 20 μL of cell suspension was diluted with 20 μL of 0.4% trypan blue. Finally, viable cells were counted within the grids on hemacytometer, and their cell viability (%) was calculated as the following Eq. (2);

$$\text{Cell viability} = \frac{\text{Total number of viable cells}}{\text{Total number of cells}} \times 100$$

2

To investigate cellular uptake behavior of ^{64}Cu -QT-NPs and ^{64}Cu -QT-NPs/BSA, the MDA-MB-231 cells were seeded onto 24-well plates (1×10^5 cells/well) and incubated at 37°C overnight under a 5% CO_2 atmosphere. 0.37 MBq of ^{64}Cu -QT-NPs and ^{64}Cu -QT-NPs/BSA were treated in each well, and then further incubated for 0.5, 2, 6, and 24 h. And then the cells were washed twice with ice-cold PBS in order to remove the remaining nanoparticles not up-taken by the cells. After that, the cells were detached with 0.1% trypsin and then its radioactivity was measured using a gamma counter (1480 WIZARD, PerkinElmer, USA). The cellular uptake rate for each ^{64}Cu -QT-NPs and ^{64}Cu -QT-NPs/BSA was represented as the percentage injected dose (%ID).

In-vivo small-animal PET imaging for ^{64}Cu -QT-NPs and ^{64}Cu -QT-NPs/BSA

All the animal experiments were performed according to the guidelines of the IACUC of the KIRAMS. The tumor-bearing animal models were produced in 6-week-old male BALB/c nude mice by subcutaneous injection of MDA-MB-231 cells (1×10^7) in the right thigh. The tumors were allowed to grow for 4 weeks until their size reached a diameter of 10–15 mm, and then the PET imaging and biodistribution studies were performed on the xenograft mice.

Each radioisotope labeled sample, ^{64}Cu -QT-NPs and ^{64}Cu -QT-NPs/BSA (~ 11.1 MBq/ 100 μL) were tail-vein injected into the tumor-bearing mice ($n = 3/\text{group}$), respectively. After 2, 6, 24 and 48 h, the mice were anesthetized with isoflurane (2%) and placed in a spread prone position to obtain PET images with a small-animal PET scanner (Inveon™, Siemens Preclinical Solutions, USA). The PET scan was performed for 30 min, and the emission data was acquired using 64 detectors in PET scanner under the condition with 350–650 keV of energy window and 3.43 ns of timing window (the difference between the late and early arrival times). All images were reconstructed using a 2-dimensionally ordered-subset expectation maximization (2D-OSEM) algorithm with 4 iterations. For image analysis, the static PET images were displayed in the coronal (or frontal) and transverse (or horizontal, axial) directions; the coronal is the vertical plane that divides the body into ventral and dorsal sections, and the transverse is the plane that divides the body into superior and inferior parts. The three-dimensional regions of interest (ROIs) were manually drawn over the tumor, lung, liver and blood pool using the Inveon Research Workplace software (IRW, Siemens Preclinical Solutions) [54].

In-vivo biodistribution for ^{64}Cu -QT-NPs and ^{64}Cu -QT-NPs/BSA

Biodistribution studies for ^{64}Cu -QT-NPs, and ^{64}Cu -QT-NPs/BSA were performed in the MDA-MB-231 xenografts. The 100 μL suspension with a radioactivity of 1.11 MBq for each sample was intravenously injected into the tumor-bearing mice ($n = 4/\text{group}$). After a given period of time from 2 to 48 h, the mice were sacrificed, and their blood, organs, and tumors were separated and weighed. The radioactivity of each organ was also measured with the gamma counter and the results were expressed as the percentage of injected dose per gram of tissue (%ID/g), according to the following Eq. (3);

$$\text{Injected dose per gram} = \frac{\text{Radioactivity of organ tissue} / \text{Injected radioactivity}}{\text{Weight of organ tissue}} \times 100$$

3

Furthermore, intact ^{64}Cu (1.11 MBq) was also injected into the BALB/c normal mice ($n = 3$) to confirm its biodistribution as a control, and the mice were sacrificed after 3 and 22 h. The organs were separated, weighed and measured its radioactivity to obtain %ID/g.

Results And Discussion

Physico-chemical characterization

To understand the physicochemical properties between the present radioisotope-labeled samples (^{64}Cu -QT-NPs and ^{64}Cu -QT-NPs/BSA), and the nonradioisotope-labeled ones (Cu-QT-NPs and Cu-QT-NPs/BSA), their differences and similarities were systematically analyzed and compared to each other as shown in Fig. 2 and Fig. S3. According to the powder X-ray diffraction (XRD) patterns (Fig. 2a and Fig. S3), all the samples exhibited a series of well-developed ($00l$) reflections, though the ($00l$) peaks for the BSA coated samples were slightly broadened along with the weakening of their intensities, due to the presence of BSA molecules between QT-NPs giving rise to a random-orientation of 2D nanoplates [55]. As discussed above, the crystal structure for both the samples of ^{64}Cu -QT-NPs and ^{64}Cu -QT-NPs/BSA showed a 2-dimensional nature as clearly evidenced by the presence of (003) and (006) peaks, indicating the formation of hydrocalcite-like structure (JPCDS no 14-0191). Their morphology and particle size were also confirmed by the SEM studies (Fig. 2b). Though the BSA coating on QT-NPs (^{64}Cu -QT-NPs/BSA and Cu-QT-NPs/BSA) gave rise to the round-shaped hexagonal, all the samples were observed to be not much different in terms of their shape and morphology of typical 2D QT-NPs. And their average particle size was determined to be ~ 75 nm. According to the dynamic light scattering (DLS) measurements, the particle size of Cu-QT-NPs was determined to be 75 ± 27 nm (PDI: 0.138) in distilled water (DW), but became aggregated to be 195 ± 115 nm (PDI: 0.347) after coating with BSA to form Cu-QT-NPs/BSA. Since the isoelectric point (IEP) of BSA is at $\text{pH} = 4.5\text{-}5.0$ [56], the negatively charged BSA molecules in water (neutral pH) could be integrated onto the positively charged Cu-QT-NPs as confirmed by the reduction in zeta potential (ξ) of Cu-QT-NPs upon BSA coating from 22.7 to 7.22 mV (Table 1). Such a nano-cluster formation of Cu-QT-NPs/BSA (~ 195 nm) can be, therefore, rationalized by the fact that globular BSA with 583 amino acids preferably interact with Cu-QT-NPs by electrostatic interaction (Table 1).

Table 1
Particle size and zeta potential for Cu-QT-NPs and Cu-QT-NPs/BSA

Samples	Particle size	Zeta potential
Cu-QT-NPs	75 nm \pm 29 *(0.138)	22.7 mV \pm 3.30
Cu-QT-NPs/BSA	195 nm \pm 115 *(0.347)	7.22 mV \pm 3.21
* PDI: Polydispersity index is shown in parentheses		

Labeling efficiency and labeling stability of ^{64}Cu radioisotope on QT-NPs

To evaluate radiolabeling efficiency of ^{64}Cu radioisotope depending on the amount of radioactivity, ^{64}Cu -QT-NPs were first prepared with different doses of radioactivity of 74, 185, 370, and 740 MBq, corresponding to 8.19, 20.49, 40.97, and 81.94 pmol of ^{64}Cu , respectively, those which were compared with ^{64}Cu -ads-QT-NPs with 185 MBq (20.49 pmol of ^{64}Cu). As expected, all the samples, except the physisorbed phase, showed very high labeling efficiencies beyond 99%, regardless of the amount of ^{64}Cu radioisotope, as shown in Fig. 3; the labeling efficiency was obtained as 99.22 ± 0.16 , 99.93 ± 0.08 , 99.04 ± 0.99 , and $99.25 \pm 0.12\%$, respectively. On the other hand, the latter, where the ^{64}Cu radioisotope was physically adsorbed on the surface of QT-NPs, was measured to be only $63.4 \pm 0.99\%$; the low chemical stability of ^{64}Cu -ads-QT-NPs could also be explained by the fact that the ^{64}Cu radioisotope was weakly bound with physical adsorption on the external surface of QT-NPs in the form of unknown copper compound, which was found to be copper hydroxychloride, as shown in the Supplementary data Fig. S4. Different from the ^{64}Cu -ads-QT-NPs sample, the ^{64}Cu radioisotope atoms in the present ^{64}Cu -QT-NPs were stabilized in the 2D QT lattice, resulting in high thermodynamic stability thanks to the gain of lattice energy as illustrated in Fig. 1a.

In the present study, the sample ^{64}Cu -QT-NPs with 740 MBq was divided into 370 MBq of ^{64}Cu -QT-NPs and 370 MBq of ^{64}Cu -QT-NPs/BSA (Fig. 1) to explore ^{64}Cu labeling efficiency and labeling stability. At first both the samples were centrifuged using filter tubes, and then radioactivities of the isolated precipitates and supernatants were measured with a radioisotope dose calibrator; the labeling efficiencies of ^{64}Cu -QT-NPs and ^{64}Cu -QT-NPs/BSA were determined to be 99.0 ± 0.99 and $99.7 \pm 0.42\%$, respectively (Fig. 4a). It was, therefore, concluded that all the $^{64}\text{Cu}^{2+}$ ions were stabilized in the 2D QT lattice without remaining in the synthesis solution. To cross-confirm the labeling efficiency for ^{64}Cu -QT-NPs and ^{64}Cu -QT-NPs/BSA, both the samples were studied on basis of radio-TLC, where the mobile phase was a 20 mM sodium citrate / 50 mM EDTA solution (pH = 5.5). As illustrated in Fig. 4b, the instant thin layer chromatograph (iTLC) paper, dropped with the radioactive sample, was placed into the mobile phase for 10 min. And then the unbound and unstable ^{64}Cu radioisotopes were removed by the mobile phase. In the case of free ^{64}Cu radioisotope, all the ^{64}Cu ions were moved to the solvent front by the mobile phase (Fig. 4c). On the other hand, the radio-TLC peaks of ^{64}Cu -QT-NPs and ^{64}Cu -QT-NPs/BSA were obtained at

the origin (starting line) as shown in Fig. 4d and 4e. However, from the radio-TLC results of ^{64}Cu -ads-QT-NPs and ^{64}Cu -ads-QT-NPs/BSA (Fig. S5), it was found that 49.1% of ^{64}Cu radioisotopes adsorbed on the former and 90.8% of them on the latter were detached, due to the fact that the ^{64}Cu radioisotopes were weakly bound on the external surface of QT-NPs as expected, and eventually removed by mobile phase easily. It is, therefore, concluded that the excellent chemical stability of ^{64}Cu radioisotope in ^{64}Cu -QT-NPs and ^{64}Cu -QT-NPs/BSA can be ensured by the isomorphical substitution of ^{64}Cu into the 2D QT lattice.

In addition, the ^{64}Cu labeling stability for each sample was investigated not only in saline and PBS but also in biological media such as mouse serum and human one, and it was found that ^{64}Cu -QT-NPs and ^{64}Cu -QT-NPs/BSA exhibited very high stability beyond 99% in all media (Fig. 5). Such a high thermodynamic stability could only be explained by the gain of lattice energy, since the ^{64}Cu radioisotopes were indeed incorporated into the octahedral sites of the QT lattice (Fig. 1).

In-vitro cytotoxicity and cellular uptake studies

Biocompatibility and toxicity of nanoparticles are one of important factors for their biomedical application. To evaluate the cell viability for QT-NPs containing ^{64}Cu radioisotope, both the samples with 0.37 MBq, ^{64}Cu -QT-NPs and ^{64}Cu -QT-NPs/BSA, were treated on the MDA-MB-231 cell lines. After incubating them for 24 h, their cell viability was observed to be almost 100%, indicating their excellent biocompatibility and chemical stability (Fig. 6a), which is also well consistent with our previous studies; QT-NPs were extremely low in toxicity as confirmed by both *in-vitro* and *in-vivo* experiments, and internalized inside the cells very efficiently *via* clathrin-mediated endocytosis [42, 43]. In this study, the *in-vitro* cytotoxicity for the non-radioactive Cu-doped samples, Cu-QT-NPs and Cu-QT-NPs/BSA, was also evaluated in the concentration range of 1–100 $\mu\text{g}/\text{mL}$ on the cell culture line of MDA-MB-231 for 24 and 48 h, and was found to be very low in toxicity (Fig. S6).

Furthermore, the *in-vitro* cellular uptake behavior for the biocompatible ^{64}Cu -labeled QT-NPs (^{64}Cu -QT-NPs and ^{64}Cu -QT-NPs/BSA) was also studied on the cell culture line of MDA-MB-231 for 24 h. As represented in Fig. 6b, the cellular uptake efficiencies (%dose/cells) of ^{64}Cu -QT-NPs and ^{64}Cu -QT-NPs/BSA were obtained as 23.0 ± 1.36 and 7.9 ± 1.24 , respectively, within 30 min, but improved remarkably as 43.3 ± 5.02 and 31.2 ± 2.44 , respectively, after 24 h, those which were higher than that of other reported radioisotope labeled samples. In the case of ^{64}Cu -DOTA conjugated dendrimers, a very low uptake efficiency of 1.11% was observed after 2 h of incubation time on human nasopharyngeal cancer (KB) cell line [57]. For ^{64}Cu -NOTA-PA1 formed by conjugating ^{64}Cu -NOTA with pasireotide derivative (PA1), its intercellular uptake efficiency was only 3.67 ± 0.36 and $2.97 \pm 0.09\%$ at 2 h on human breast cancer (MCF-7) and human lung cancer (A549) cell lines, respectively [58]. In the case of ^{64}Cu -Sur-NGR2, ^{64}Cu -labeled dimeric NGR (asparagine-glycine-arginine) peptide based on sarcophagine (Sur) cage, its uptake value was observed to be 0.72 ± 0.01 and $1.72 \pm 0.24\%$ upon treating on the human fibrosarcoma (HT-1080) cell line at 1 h and 2 h, respectively, after incubation [59]. We, therefore, came up with a conclusion that our designed samples, ^{64}Cu -QT-NPs and ^{64}Cu -QT-NPs/BSA, can be a promising radioisotope delivery and

imaging technology platform not only because of their high labeling efficiency and excellent chemical stability, but also because of their extremely high biocompatibility and low toxicity.

In-vivo PET imaging and biodistribution studies

To demonstrate the targeting property of ^{64}Cu -QT-NPs and ^{64}Cu -QT-NPs/BSA in *in-vivo*, the PET imaging and biodistribution studies were carried out on the MDA-MB-231 tumor-bearing xenograft mouse model (Fig. 7 and Fig. 8); they were visualized using a small-animal PET scanner (Inveon™), where the reconstructed images could be made by detecting gamma rays (energy, 511 keV) generated from the decay of ^{64}Cu radioisotopes (${}_{29}^{64}\text{Cu} \rightarrow {}_{28}^{64}\text{Ni} + {}_1^0\beta(\text{positron}) + \nu_e(\text{neutrino})$) [60, 61] as shown in Fig. 7a and 7b. The coronal and transverse PET images were made at various progressive time using a PET scanner, and then the time activity curves for tumors, muscles, liver, and blood were obtained by performing the quantitative region-of-interest (ROI) analysis as shown in Fig. 7c and 7d and Table S2. A prompt and persistent uptake of nanoplates into tumor tissues was achieved in both cases due to the passive targeting effect of QT-NPs (50 to 200 nm) as well described as the enhanced permeability and retention (EPR) effect. Therefore the tumor region (white dot circles and yellow arrow) in PET images becomes brighter for both, but the image of ^{64}Cu -QT-NPs/BSA appears to be much brighter than that of ^{64}Cu -QT-NPs with respect to the time. As presented in Fig. 8a and Table S2, the ^{64}Cu -QT-NPs contents uptaken by tumor tissues and cells were increased gradually from 0.71 ± 0.10 , 1.40 ± 0.29 , and 2.13 ± 0.25 , to 2.43 ± 0.60 %ID/g with respect to the given time (2, 6, 24, and 48 h). After BSA coating, however, ^{64}Cu -QT-NPs/BSA seemed to be more efficiently uptaken by tumor tissues, since their contents were even more increased from 0.96 ± 0.36 to 1.80 ± 0.20 , and 4.53 ± 0.51 , to 4.93 ± 0.81 %ID/g with respect to the same period of time of 2, 6, 24, and 48 h, indicating that the BSA coated sample exhibited 2-fold higher than the uncoated after 24 h from the injection. Such a difference could be explained by the fact that the blood circulation time of ^{64}Cu -QT-NPs was surely improved by the BSA coating. In practice, %ID/g of ^{64}Cu -QT-NPs in blood pool was observed to be 0.55 ± 0.03 , 0.56 ± 0.03 , 0.55 ± 0.10 , and 0.45 ± 0.02 for 2, 6, 24 and 48 h, respectively, while that of ^{64}Cu -QT-NPs/BSA was measured to be 0.70 ± 0.10 , 0.93 ± 0.18 , 1.25 ± 0.10 , and 1.23 ± 0.19 , respectively, for the same period of time. This is an evidence that the uptake of ^{64}Cu -QT-NPs/BSA in tumor tissues was more efficiently made after BSA coating due to the enhanced blood circulation time. In addition, the tumor-to-liver ratio (%) of ^{64}Cu -QT-NPs/BSA (21.86 ± 5.05 %) was also examined to check its targeting function, and was found to be 1.7-fold higher than that of ^{64}Cu -QT-NPs (12.67 ± 6.38 %) after 48 h from the injection (Fig. 8b). It is surely due to an enhanced colloidal stability of Cu-QT-NPs/BSA (186 ± 38 nm of size distribution in saline, PDI: 0.356) compared to Cu-QT-NPs (585 ± 102 nm of size distribution in saline, PDI: 0.669) as shown in Table S3. From the above results, the particle size of ^{64}Cu -QT-NPs/BSA could also be expected to be ~ 200 nm in the blood enabling the enhanced tumor penetration by the EPR effect. And it is, therefore, not that surprising that the BSA coated, ^{64}Cu -QT-NPs/BSA, showed 2-fold higher tumor uptake rate than ^{64}Cu -QT-NPs.

Even though the present radio-labeled samples, ^{64}Cu -QT-NPs and ^{64}Cu -QT-NPs/BSA, could effectively deliver the radioisotopes to tumor tissues, thanks to the passive targeting effect, there were some toxicity

issues due to a high uptake rate in the liver. After intravenous administration of inorganic nanoparticles within the size of 10 ~ 200 nm, they were known to be rapidly sequestered from the blood and severely accumulated in reticuloendothelial system (RES) organs including liver, spleen, and lymph nodes [62–64]. Thus the liver uptake and clearance of injected nanoparticles have been usually considered as major concerns for bio-applications. Therefore, the U.S. Food and Drug Administration (FDA) regulates that all injected agents have to be cleared completely in a reasonable period of time [62–64]. According to the present *in-vivo* biodistribution study for ^{64}Cu -QT-NPs and ^{64}Cu -QT-NPs/BSA as shown in Fig. 9, the uptake rates into liver for the former ($49.1 \pm 8.7\% \text{ID/g}$) and the latter ($49.5 \pm 8.0\% \text{ID/g}$) were determined to be rather high at 2 h after injection, but decreased respectively to 58.0 and 56.4% after 48 h in liver, resulting in 20.6 ± 3.7 and $21.6 \pm 3.1\% \text{ID/g}$, respectively. And the uptake rates into spleen for the former ($134.1 \pm 51.1\% \text{ID/g}$) and the latter ($88.9 \pm 41.4\% \text{ID/g}$) were also reduced down to 58.9 and 68.2% after 48 h, giving rise to 55.0 ± 31.8 and $28.3 \pm 3.6\% \text{ID/g}$, respectively. As well documented [62], inorganic nanoparticles could be mainly trapped in the reticuloendothelial system (RES) organs (liver and spleen) in the beginning, and then significantly decreased over time due to the excretion mechanism by hepatic (bile to feces) pathway. As expected, the present samples, ^{64}Cu -QT-NPs and ^{64}Cu -QT-NPs/BSA, were uptaken more into liver and spleen than the other organs (Fig. 7 and Fig. 9). In addition, intact ^{64}Cu ions (free ^{64}Cu radioisotopes from $^{64}\text{CuCl}_2$) were also uptaken up into liver tissues but usually cleared within 24 h by the renal (kidney) clearance (Fig. S6).

Nevertheless, the liver uptake of ^{64}Cu -QT-NPs and ^{64}Cu -QT-NPs/BSA over 24 h may be posed its toxicity, which is always one of the major concern for the use of nanoparticles in nanomedicine [63]. However, according to our previous *in-vivo* liver toxicity results for QT-NPs as summarized in Table S4, the serum levels of alanine aminotransferase (ALT) and aspartate aminotransferase (AST), as the recognition index of liver toxicity, liver disease, or liver damage, were found to be within the normal ranges (7-227 and 37–329 U/L for ALT and AST, respectively) after 72 h from the intraperitoneal administration of QT-NPs [44], indicating the biocompatibility and non-toxicity of the present samples, ^{64}Cu -QT-NPs and ^{64}Cu -QT-NPs/BSA. Furthermore, the concentrations of Mg and Al ions, the major elements of QT, found in liver tissue for the QT treated animal group were determined to be very similar with those for the QT non-treated one at one week after the final injection (Table S3) [44]. As described above, the uptake rate in liver for ^{64}Cu -QT-NPs and ^{64}Cu -QT-NPs/BSA was decreased ~ 60% from 2 to 48 h after injection, expecting its clearance further from the body over time. We, therefore, propose that the present biocompatible nanoplates, ^{64}Cu -QT-NPs and ^{64}Cu -QT-NPs/BSA, could be the promising new nanoagent for PET imaging.

Conclusions

We were successful in preparing ^{64}Cu -QT-NPs based on the co-precipitation and subsequent hydrothermal reaction as the two-step processes. The divalent ^{64}Cu radioisotope was isomorphically substituted in the octahedral site of the 2D QT lattice to form ^{64}Cu -QT-NPs, which showed excellent labeling efficiency and stability, cellular uptake efficiency and biocompatibility even after the BSA

treatment, suggesting its potential as a PET imaging agent. According to the present *in-vivo* PET imaging experiments, both the radioisotope labeled samples, ^{64}Cu -QT-NPs and ^{64}Cu -QT-NPs/BSA, were selectively targeted to the tumor tissues. One more thing to note here is that the latter, the BSA coated, showed 2-fold higher uptake rate in tumor tissues than the former surely due to an enhanced colloidal stability eventually leading to the longer blood circulation when injected, and as a consequence, the better EPR effect. Moreover, the present 2D QT-NPs were determined to be excreted over time by hepatic pathway after intravenous administration. Therefore, the present samples, ^{64}Cu -QT-NPs and ^{64}Cu -QT-NPs/BSA, can be proposed as the alternative to escape from the toxicity issue of nanoparticles in nanomedicine, thanks to its high labeling efficiency and labeling stability as well as biocompatibility. So we conclude that both phases are surely the promising candidates as radionuclides delivery nano-devices not only for PET imaging but also for radiotherapy as the nanomedicine. Nevertheless, further studies are still required to understand their long-term stability and toxicology in *in-vivo*, and the enhanced tumor uptake behaviors for the radioisotope doped phases conjugated with some passive and active targeting agents (folate, antigen, etc.) eventually to establish the radioisotope-labeled QT platform technology, which will be made in the very near future.

Declarations

Acknowledgments

The authors would like to thank Dr. Kyo Chul Lee, Dr. Jung Young Kim, and Mr. Hyun Park in KIRAMS for production of ^{64}Cu .

Authors' contributions

Sairan Eom: Methodology, Investigation, Formal analysis, Visualization, Writing – original draft, Writing - review & editing. Min Hwan Kim: Investigation, Formal analysis. Ranji Yoo: Investigation. Goeun Choi: Investigation, Writing - review & editing, Project administration, Funding acquisition. Joo Hyun Kang: Project administration. Yong Jin Lee: Conceptualization, Supervision, Writing – review. Jin-Ho Choy: Supervision, Project administration, Funding acquisition, Conceptualization, Writing - review & editing.

Funding

This research was supported by Basic Science Research Program through the National Research Foundation of Korea (NRF) funded by the Ministry of Education (No. 2020R11A2074844), by the NRF grant funded by the Korea government (MSIT) (No. 2020R1F1A1075509), and under the framework of the International Cooperation Program managed by NRF (2017K2A9A2A10013104). This study was also partly supported by a grant from the Korea Institute of Radiological and Medical Sciences (KIRAMS), by the Ministry of Science and ICT (MSIT), the Republic of Korea (No. 50536–2022).

Availability of data and materials

All data generated or analyzed during this study are included in this published article.

Competing interests

The authors declare that they have no competing interests.

Consent for publication

Not applicable.

Ethics approval and consent to participate

All experimental procedures involving animals were conducted in strict accordance with the appropriate institutional guidelines for animal research. The protocol was approved by the Committee on the Ethics of Animal Experiments of the KIRAMS (Approval Number: kirams2017-0091 and kirams2019-0076).

References

1. Wang C, Ding S, Wang S, Shi Z, Pandey NK, Chudal L, et al. Endogenous tumor microenvironment-responsive multifunctional nanoplatfoms for precision cancer theranostics. *Coord Chem Rev.* 2021;426:213529.
2. Ge J, Zhang Q, Zeng J, Gu Z, Gao M. Radiolabeling nanomaterials for multimodality imaging: New insights into nuclear medicine and cancer diagnosis. *Biomaterials.* 2020; 228:119553.
3. Liang L, Chen N, Jia Y, Ma Q, Wang J, Yuan Q, et al. Recent progress in engineering near-infrared persistent luminescence nanoprobcs for time-resolved biosensing/bioimaging. *Nano Res.* 2019;12:1279–1292.
4. Caracciolo G, Vali H, Moore A, Mahmoudi M. Challenges in molecular diagnostic research in cancer nanotechnology. *Nano Today.* 2019;27:6–10.
5. Hu Y, Mignani S, Majoral JP, Shen M, Shi X. Construction of iron oxide nanoparticle-based hybrid platforms for tumor imaging and therapy. *Chem Soc Rev.* 2018;47:1874–1900.
6. Jo SD, Ku SH, Won YY, Kim SH, Kwon IC. Targeted nanotheranostics for future personalized medicine: recent progress in cancer therapy. *Theranostics.* 2016;6:1362–1377.
7. Lee DE, Koo H, Sun IC, Ryu JH, Kim K, Kwon IC. Multifunctional nanoparticles for multimodal imaging and theragnosis. *Chem Soc Rev.* 2012;41:2656–2672.
8. Brigger I, Dubernet C, Couvreur P. Nanoparticles in cancer therapy and diagnosis. *Adv Drug Deliv Rev.* 2012;64:24–36.
9. Fass L, Imaging and cancer: A review. *Mol Oncol.* 2008;2:115–152.
10. Pérez-Medina C, Teunissen AJ, Kluza E, Mulder WJ, Van der Meel R. Nuclear imaging approaches facilitating nanomedicine translation. *Adv Drug Del Rev.* 2020;154–155:123–141.

11. Chopra D. Radiolabelled nanoparticles for diagnosis and treatment of cancer. In: Shingh N, editor. Radioisotopes-applications in bio-medical science. London: IntechOpen; 2011. p. 226.
12. Bariwal J, Ma H, Altenberg GA, Liang H. Nanodiscs: a versatile nanocarrier platform for cancer diagnosis and treatment. *Chem Soc Rev.* 2022; DOI: 10.1039/D1CS01074C.
13. Lee W, Sarkar S, Pal R, Kim JY, Park H, Huynh PT, et al. Successful application of CuAAC click reaction in constructing ^{64}Cu -labeled antibody conjugates for immuno-PET imaging. *ACS Appl Bio Mater.* 2021;4:2544–2557.
14. Ma W, Fu F, Zhu J, Huang R, Zhu Y, Liu Z, et al. ^{64}Cu -Labeled multifunctional dendrimers for targeted tumor PET imaging. *Nanoscale.* 2018;10:6113–6124.
15. El-Ghareb WI, Swidan MM, Ibrahim IT, Abd El-Bary A, Tadros MI, Sakr TM. $^{99\text{m}}\text{Tc}$ -doxorubicin-loaded gallic acid-gold nanoparticles ($^{99\text{m}}\text{Tc}$ -DOX-loaded GA-Au NPs) as a multifunctional theranostic agent. *Int J Pharm.* 2020;586:119514.
16. Pellico J, Lechuga-Vieco AV, Almarza E, Hidalgo A, Mesa-Nuñez C, Fernández-Barahona I, et al. In vivo imaging of lung inflammation with neutrophil-specific ^{68}Ga nano-radiotracer. *Sci Rep.* 2017;7:1–10.
17. Tsiapa I, Efthimiadou EK, Fragogeorgi E, Loudos G, Varvarigou AD, Bouziotis P, et al. $^{99\text{m}}\text{Tc}$ -labeled aminosilane-coated iron oxide nanoparticles for molecular imaging of $\alpha_v\beta_3$ -mediated tumor expression and feasibility for hyperthermia treatment. *J Colloid Interface Sci.* 2014;433:163–175.
18. Thorp-Greenwood FL, Coogan MP. Multimodal radio-(PET/SPECT) and fluorescence imaging agents based on metallo-radioisotopes: current applications and prospects for development of new agents. *Dalton Trans.* 2011;40:6129–6143.
19. Kim KI, Jang SJ, Park JH, Lee YJ, Lee TS, Woo KS, et al. Detection of increased ^{64}Cu uptake by human copper transporter 1 gene overexpression using PET with $^{64}\text{CuCl}_2$ in human breast cancer xenograft model. *J Nucl Med.* 2014;55:1692–1698.
20. Li X, Xiong Z, Xu X, Luo Y, Peng C, Shen M, et al. $^{99\text{m}}\text{Tc}$ -labeled multifunctional low-generation dendrimer-entrapped gold nanoparticles for targeted SPECT/CT dual-mode imaging of tumors. *ACS Appl Mater Interfaces.* 2016;8:19883–19891.
21. Mitchell N, Kalber TL, Cooper MS, Sunassee K, Chalker SL, Shaw KP, et al. Incorporation of paramagnetic, fluorescent and PET/SPECT contrast agents into liposomes for multimodal imaging. *Biomaterials.* 2013;34:1179–1192.
22. Sandiford L, Phinikaridou A, Protti A, Meszaros LK, Cui X, Yan Y, et al. Bisphosphonate-anchored PEGylation and radiolabeling of superparamagnetic iron oxide: long-circulating nanoparticles for in vivo multimodal (T1 MRI-SPECT) imaging. *ACS Nano.* 2012;7:500–512.
23. Blower PJ, Lewis JS, Zweit J. Copper radionuclides and radiopharmaceuticals in nuclear medicine. *Nucl Med Biol.* 1996;23:957–980.
24. Bhattacharyya S, Dixit M. Metallic radionuclides in the development of diagnostic and therapeutic radiopharmaceuticals. *Dalton Trans.* 2011;40:6112–6128.

25. Kim JY, Park H, Lee JC, Kim KM, Lee KC, Ha HJ, et al. A simple Cu-64 production and its application of Cu-64 ATSM. *Appl Radiat Isot.* 2009;67:1190–1194.
26. McCarthy DW, Shefer RE, Klinkowstein RE, Bass LA, Margeneau WH, Cutler CS, et al. Efficient production of high specific activity ^{64}Cu using a biomedical cyclotron. *Nucl Med Biol.* 1997;24:35–43.
27. Kume M, Carey PC, Gaehle G, Madrid E, Voller T, Margenau W, et al. A semi-automated system for the routine production of copper-64. *Appl Radiat Isot.* 2012;70:1803–1806.
28. Zhao Y, Sultan D, Detering L, Cho S, Sun G, Pierce R, et al. Copper-64-alloyed gold nanoparticles for cancer imaging: improved radiolabel stability and diagnostic accuracy. *Angew Chem Int Ed.* 2014;53:156–159.
29. Zhou M, Zhang R, Huang M, Lu W, Song S, Melancon MP, et al. A chelator-free multifunctional [^{64}Cu]CuS nanoparticle platform for simultaneous micro-PET/CT imaging and photothermal ablation therapy. *J Am Chem Soc.* 2010;132:15351–15358.
30. Banerjee SR, Pullambhatla M, Foss CA, Nimmagadda S, Ferdani R, Anderson CJ, et al. ^{64}Cu -labeled inhibitors of prostate-specific membrane antigen for PET imaging of prostate cancer. *J Med Chem.* 2014;57:2657–2669.
31. Ghosh SC, Pinkston KL, Robinson H, Harvey BR, Wilganowski N, Gore K, et al. Comparison of DOTA and NODAGA as chelators for ^{64}Cu -labeled immunoconjugates. *Nucl Med Biol.* 2015;42:177–183.
32. Liu Y, Welch WJ. Nanoparticles labeled with positron emitting nuclides: advantages, methods, and applications. *Bioconju Chem.* 2012;23:671–682.
33. Liu S. Bifunctional coupling agents for radiolabeling of biomolecules and target-specific delivery of metallic radionuclides. *Adv Drug Deliv Rev.* 2008;60:1347–1370.
34. Choy JH, Kwak SY, Park JS, Jeong YJ. Cellular uptake behavior of [γ - ^{32}P] labeled ATP-LDH nanohybrids. Electronic supplementary information (ESI) available: histogram for Mg solubility of $\text{Mg}_2\text{Al-LDH}$ as a function of pH; FITC-LDH exchange rate according to NaCl concentration (FITC= fluorescein 5-isothiocyanate); cytotoxicity test of $\text{Mg}_2\text{Al-NO}_3^-$ -LDH. *J Mater Chem.* 2001;11:1671–1674.
35. Oh JM, Choi SJ, Lee GE, Han SH, Choy JH. Inorganic drug-delivery nanovehicle conjugated with cancer-cell-specific ligand. *Adv Funct Mater.* 2009;19:1617–1624.
36. Choi SJ, Choi GE, Oh JM, Oh YJ, Park MC, Choy JH. Anticancer drug encapsulated in inorganic lattice can overcome drug resistance. *J Mater Chem.* 2010;20:9463–9469.
37. Choi G, Piao H, Kim MH, Choy JH. Enabling nanohybrid drug discovery through the soft chemistry telescope. *Ind Eng Chem Res.* 2016;55:11211–11224.
38. Choi G, Choy JH. Recent progress in layered double hydroxides as a cancer theranostic nanoplatform. *Wiley Interdiscip Rev Nanomed Nanobiotechnol.* 2021;13:e1679.
39. Liu J, Harrison R, Zhou JZ, Liu TT, Yu C, Lu GQ, et al. Synthesis of nanorattles with layered double hydroxide core and mesoporous silica shell as delivery vehicles. *J Mater Chem.* 2011;21:10641–

10644.

40. Bao H, Yang J, Huang Y, Xu ZP, Hao N, Wu Z, et al. Synthesis of well-dispersed layered double hydroxide core@ ordered mesoporous silica shell nanostructure (LDH@mSiO₂) and its application in drug delivery. *Nanoscale*. 2011;3:4069–4073.
41. Khan AI, O'Hare D. Intercalation chemistry of layered double hydroxides: recent developments and applications. *J Mater Chem*. 2002;12:3191–3198.
42. Cavani F, Trifirò F, Vaccari A. Hydrotalcite-type anionic clays: Preparation, properties and applications. *Catal Today*. 1991;11:173–301.
43. De Roy A, Forano C, Besse JP. Layered double hydroxides: Synthesis and post-synthesis modification. In: Rives V, editor. *Layered double hydroxides: present and future*. New York: Nova Publishers; 2001. p. 1–39.
44. Choi G, Kwon OJ, Oh Y, Yun CO, Choy JH. Inorganic nanovehicle targets tumor in an orthotopic breast cancer model. *Sci Rep*. 2014;4:1–7.
45. Choi SJ, Oh JM, Chung HE, Hong SH, Kim IH, Choy JH. In vivo anticancer activity of methotrexate-loaded layered double hydroxide nanoparticles. *Curr Pharm Des*. 2013;19:7196–7202.
46. Choy JH, Kwak SY, Park JS, Jeong YJ, Portier J. Intercalative nanohybrids of nucleoside monophosphates and DNA in layered metal hydroxide. *J Am Chem Soc*. 1999;121:1399–1400.
47. Choy JH, Kwak SY, Jeong YJ, Park JS. Inorganic layered double hydroxides as nonviral vectors. *Angew Chem Int Ed*. 2000;39:4041–4045.
48. Choy JH, Oh JM, Park M, Shon KM, Kim JW. Inorganic–biomolecular hybrid nanomaterials as a genetic molecular code system. *Adv Mater*. 2004;16:1181–1184.
49. Park DH, Cho J, Kwon OJ, Yun CO, Choy JH. Biodegradable inorganic nanovector: passive versus active tumor targeting in siRNA transportation. *Angew Chem Int Ed*. 2016;55:4582–4586.
50. Choi G, Jeon IR, Piao H, Choy JH. Highly condensed boron cage cluster anions in 2d carrier and its enhanced antitumor efficiency for boron neutron capture therapy. *Adv. Funct Mater*. 2017;28:1704470.
51. Shi S, Fliss BC, Gu Z, Zhu Y, Hong H, Valdovinos HF, et al. Chelator-free labeling of layered double hydroxide nanoparticles for in vivo PET imaging. *Sci Rep*. 2015;5:16930.
52. Kim TH, Lee JY, Kim MK, Park JH, Oh JM. Radioisotope Co-57 incorporated layered double hydroxide nanoparticles as a cancer imaging agent. *RSC Adv*. 2016;6:48415–48419.
53. Kim JY. The development of medical radioisotopes and their labeling Studies. Degree Thesis. Hankuk University of Foreign Studies; 2010.
54. Kim MH, Woo SK, Kim KI, Lee TS, Kim CW, Kang JH. Simple methods for tracking stem cells with ⁶⁴Cu-labeled DOTA-hexadecyl-benzoate. *ACS Med Chem Lett*. 2015;6:528–530.
55. Widjonarko N. Introduction to advanced x-ray diffraction techniques for polymeric thin films. *Coatings*. 2016;6:54.

56. Phan HT, Bartelt-Hunt S, Rodenhausen KB, Schubert M, Bartz JC. Investigation of bovine serum albumin (BSA) attachment onto self-assembled monolayers (SAMs) using combinatorial quartz crystal microbalance with dissipation (QCM-D) and spectroscopic ellipsometry (SE). *PloS One*. 2015;10:e0141282.
57. Ma W, Fu F, Zhu J, Huang R, Zhu Y, Liu Z, et al. ^{64}Cu -Labeled multifunctional dendrimers for targeted tumor PET imaging. *Nanoscale*. 2018;10:6113–6124.
58. Liu F, Guo X, Liu T, Xu X, Li N, Xiong C, et al. Evaluation of Pan-SSTRs targeted radioligand [^{64}Cu] NOTA-PA1 using micro-PET imaging in xenografted mice. *ACS Med Chem Lett*. 2020;11:445–450.
59. Li G, Wang X, Zong S, Wang J, Conti PS, Chen K. MicroPET imaging of CD13 expression using a ^{64}Cu -labeled dimeric NGR peptide based on sarcophagine cage. *Mol Pharm*. 2014;11:3938–3946.
60. Niccoli Asabella A, Cascini GL, Altini C, Paparella D, Notaristefano A, Rubini G. The copper radioisotopes: a systematic review with special interest to ^{64}Cu . *BioMed Res Int*. 2014;2014:1–9.
61. Eom S, Choi G, Nakamura H, Choy JH. 2-Dimensional nanomaterials with imaging and diagnostic functions for nanomedicine; A review. *Bull Chem Soc Jap*. 2020;93:1–12.
62. Yu M, Zheng J. Clearance pathways and tumor targeting of imaging nanoparticles. *ACS Nano*. 2015;9:6655–6674.
63. Yang G, Phua SZF, Bindra AK, Zhao Y. Degradability and clearance of inorganic nanoparticles for biomedical applications. *Adv Mater*. 2019;31:1805730.
64. Choi HS, Liu W, Misra P, Tanaka E, Zimmer JP, Ipe BI, et al. Renal clearance of nanoparticles. *Nat Biotechnol*. 2007;25:1165–1170.

Figures

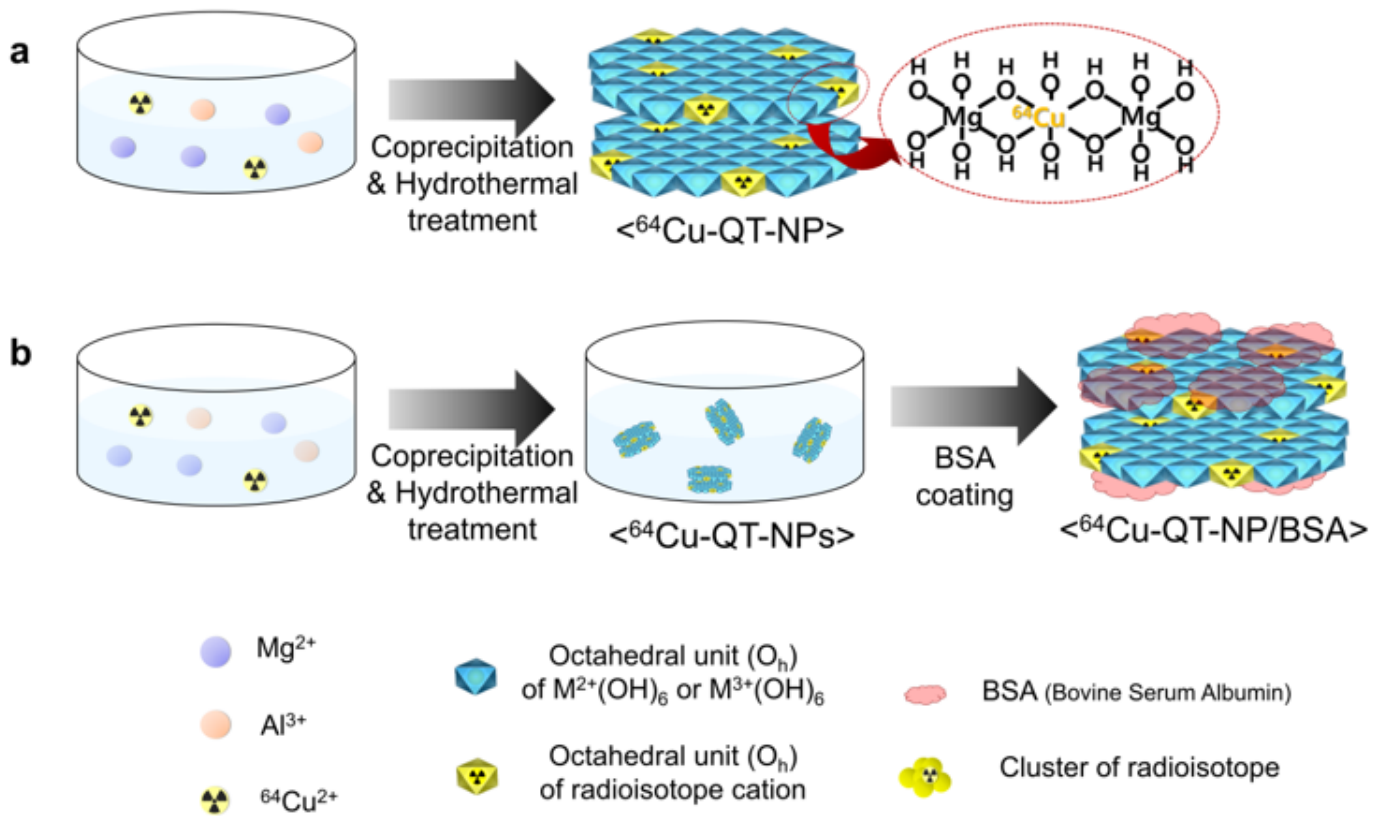


Figure 1

Structural schemes for the isomorphically substituted ${}^{64}\text{Cu}$ in the QT lattice of **a** ${}^{64}\text{Cu-QT-NP}$, and its BSA coated **b** ${}^{64}\text{Cu-QT-NP/BSA}$

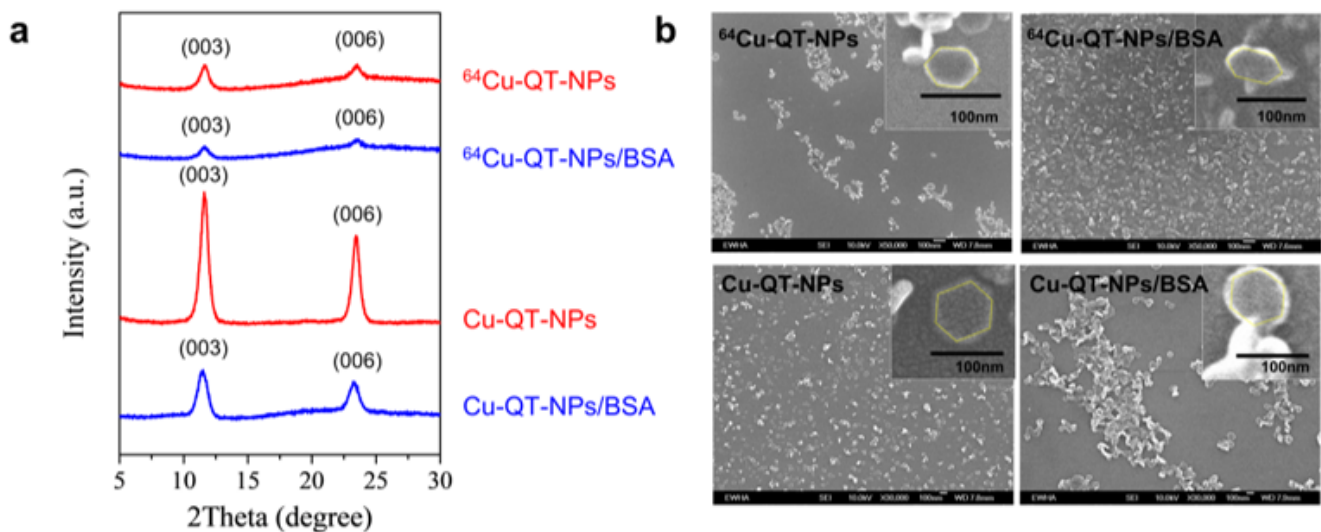


Figure 2

a Powder XRD patterns and **b** SEM images of ^{64}Cu -QT-NPs, ^{64}Cu -QT-NPs/BSA, Cu-QT-NPs and Cu-QT-NPs/BSA

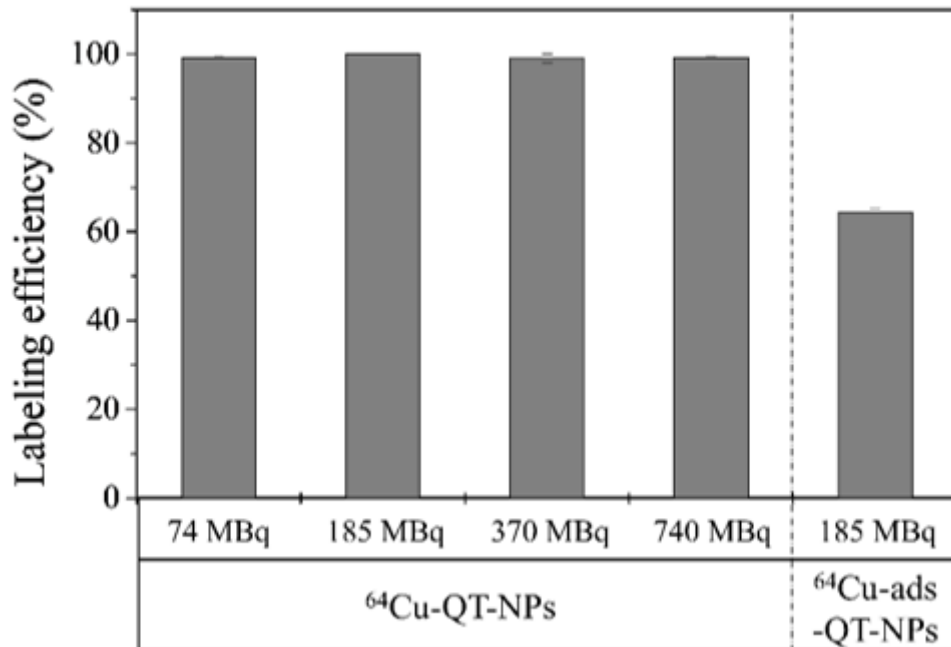


Figure 3

Differences in labeling efficiency (%) of ^{64}Cu between the isomorphically substituted (^{64}Cu -QT-NPs) and the physisorbed (^{64}Cu -ads-QT-NPs) with respect to the content of radioactivity

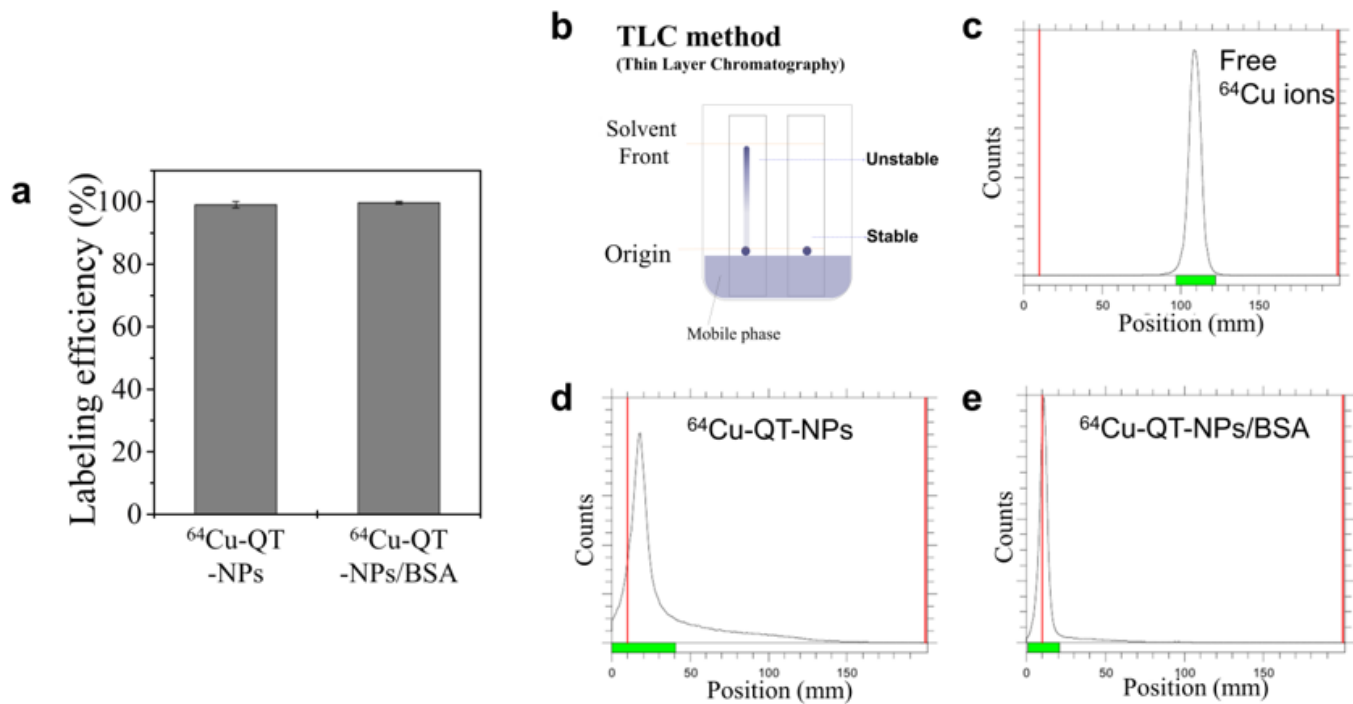


Figure 4

a Labeling efficiency of ^{64}Cu -QT-NPs and ^{64}Cu -QT-NPs/BSA. **b** Illustration for the radio-thin-layer chromatography (radio-TLC) method, and radio-TLC graphs of **c** free ^{64}Cu ions, **d** ^{64}Cu -QT-NPs, and **e** ^{64}Cu -QT-NPs/BSA

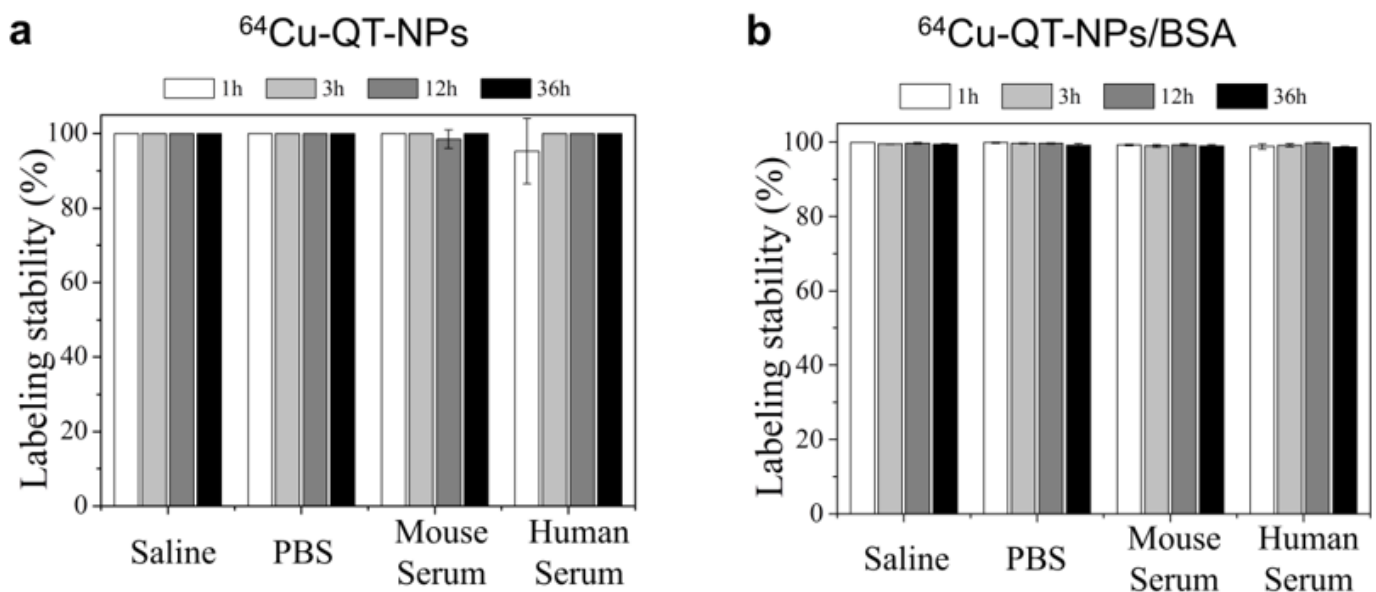


Figure 5

Labeling stability of **a** ^{64}Cu -QT-NPs and **b** ^{64}Cu -QT-NPs/BSA in saline, PBS, mouse and human serums

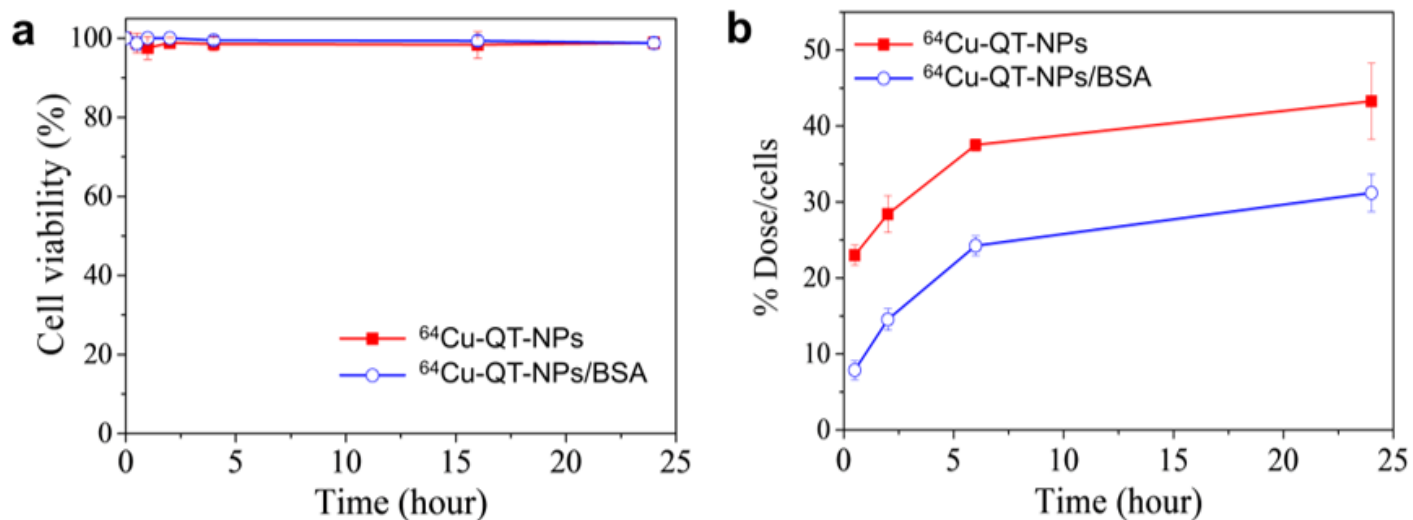


Figure 6

a Cell viability of ^{64}Cu -QT-NPs and ^{64}Cu -QT-NPs/BSA with the radioactivity of 0.37 MBq on the human breast cancer cell line (MDA-MB-231) for 24 h. **b** *In-vitro* cellular uptake rate for ^{64}Cu -QT-NPs and ^{64}Cu -QT-NPs/BSA on the same cell line with respect to time

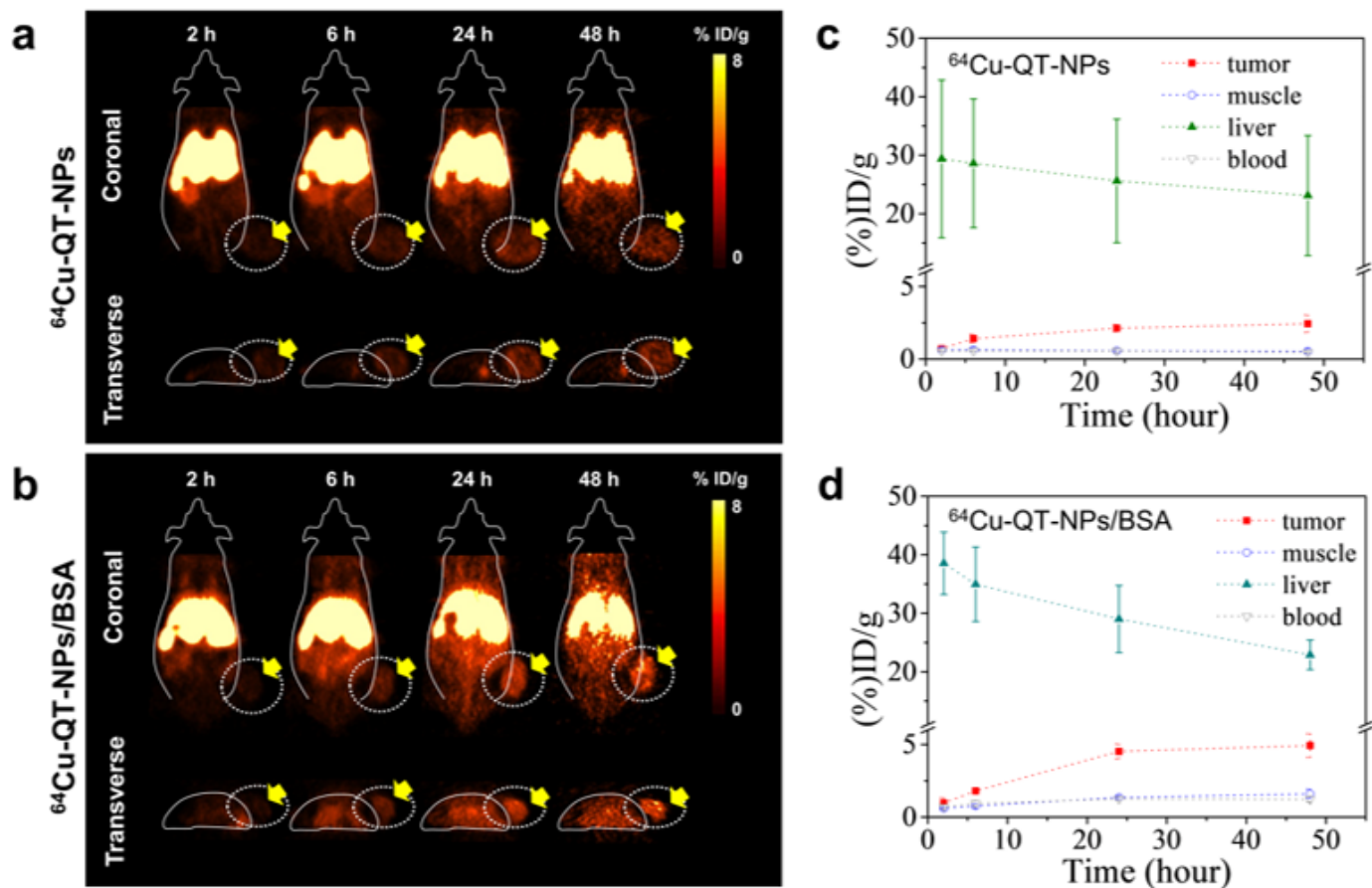


Figure 7

In-vivo positron emission tomography (PET) images for **a** ^{64}Cu -QT-NPs and **b** ^{64}Cu -QT-NPs/BSA on the MDA-MB-231 xenograft mice model after *i.v.* injection. (Tumor region: white-dotted circles indicated with yellow arrow). Time activity curves and mean values \pm SD ($n = 3$) for the tumor, muscle, liver and blood for **c** ^{64}Cu -QT-NPs and **d** ^{64}Cu -QT-NPs/BSA

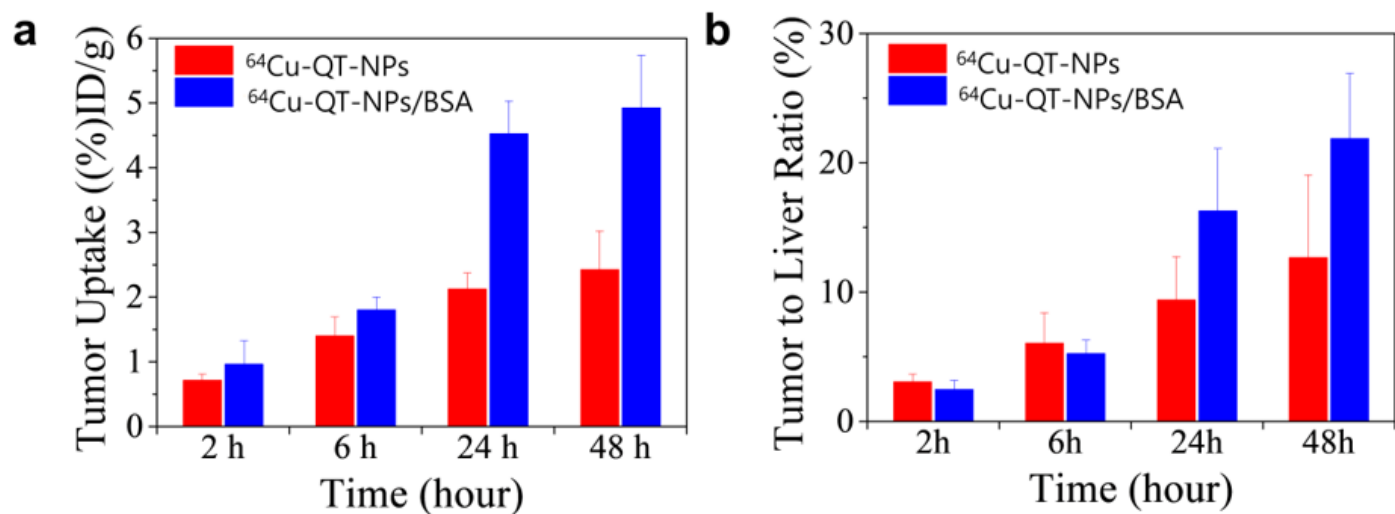


Figure 8

a The uptake rate by tumor tissues, and **b** the tumor to liver ratio (%) for ^{64}Cu -QT-NPs and ^{64}Cu -QT-NPs/BSA, respectively on the MDA-MB-231 xenograft mice model at 2, 6, 24, and 48 h after the injection

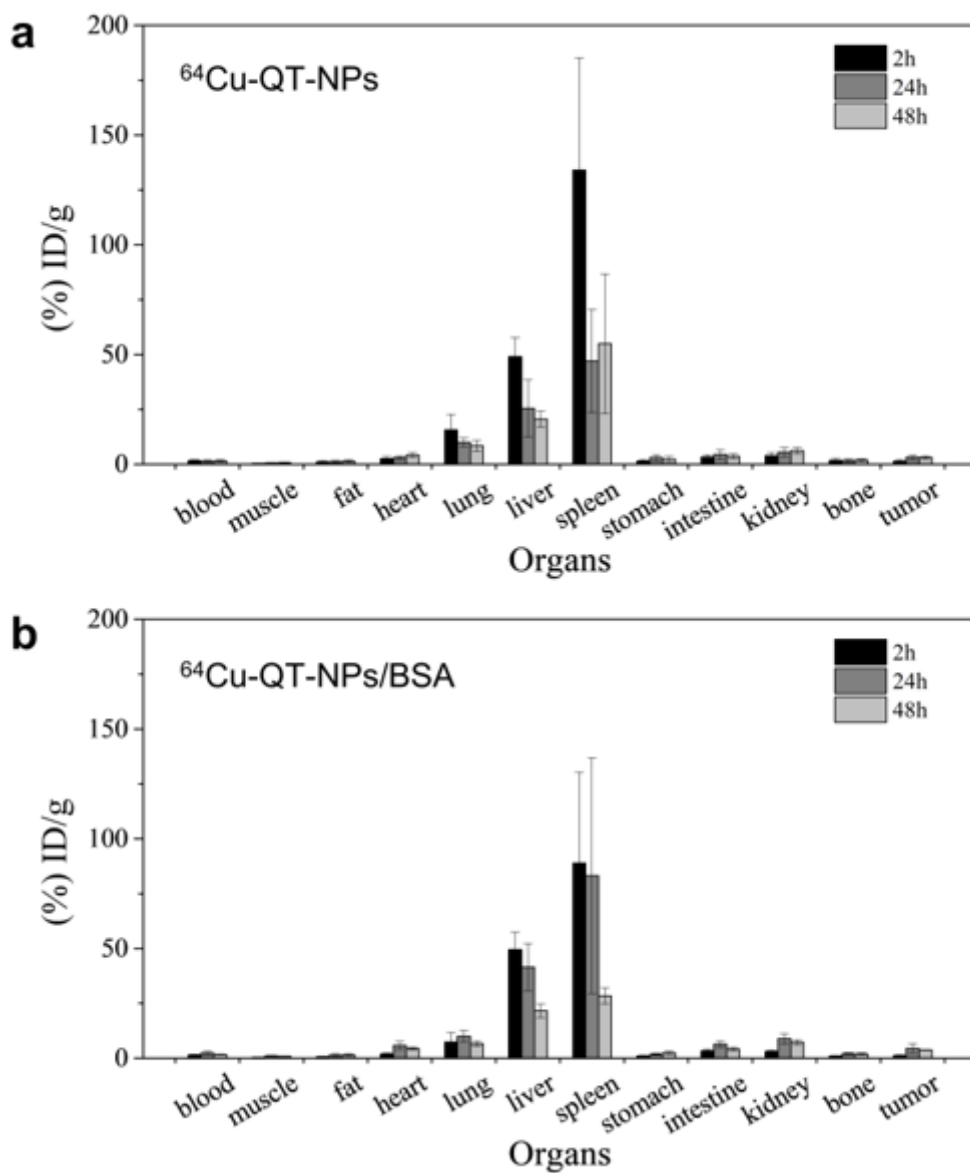


Figure 9

In-vivo biodistribution data for **a** ^{64}Cu -QT-NPs and **b** ^{64}Cu -QT-NPs/BSA were collected 2, 24, and 48 h after being *i.v.* injected on human breast cancer (MDA-MB-231) xenograft mice model ($n = 4$). The %ID/g for each organ was calculated using Equation (3)

Supplementary Files

This is a list of supplementary files associated with this preprint. Click to download.

- [JNanotechnolSupplementary64CuQTNPsProf.Choy.pdf](#)